Polymer Testing 104 (2021) 107405

Contents lists available at ScienceDirect

Polymer Testing

journal homepage: www.elsevier.com/locate/polytest

PLA toughening via bamboo-inspired 3D printed structural design

Juraj Svatík [a,*], Petr Lepcio [a], František Ondreáš [a,b], Klára Zárybnická [a], Marek Zbončák [a], Přemysl Menčík [c], Josef Jančář [a,c]

[a] Central European Institute of Technology, Brno University of Technology, Purkyňova 656/123, 612 00, Brno, Czech Republic
[b] Contipro a.s., Dolni Dobrouč 401, 561 02, Dolni Dobrouč, Czech Republic
[c] Faculty of Chemistry, Brno University of Technology, Purkyňova 118, 612 00, Brno, Czech Republic

ARTICLE INFO

Keywords:
Porosity gradient
3D printing
PLA toughening
Polymer foams
Cellular structures

ABSTRACT

Bioinspired structures can attain mechanical properties unseen in conventional artificial materials. Specifically, the introduction of a cellular structure with a precisely designed distribution of cells, cell sizes, and cell walls is expected to enhance the mechanical response. Polylactic acid (PLA) is a biodegradable polymer produced from renewable resources with very interesting properties and good three-dimensional (3D) printing processability. However, its embrittlement during ageing at room temperature after a very short period of time (a few hours) significantly reduces its usability for advanced applications. Intense effort has been invested in improving its toughness via composition modification. However, this approach can worsen some other properties, make processing more difficult, and increase the carbon footprint. Therefore, fused deposition modelling (FDM) 3D printing was used to manufacture porous bamboo-inspired structures of unmodified PLA. The toughening of PLA solely by the pore gradient, which controlled the energy dissipation mechanism, was introduced for the first time. Improvement of the ductility and work at break was observed especially for notched specimens. Prevention of catastrophic failure could enable the use of gradient porous materials in structural components. The fundamental relationships and practical hints resulting from the work provide a foundation for the future design of toughened 3D printed structures.

1. Introduction

Development of functional foams focuses on a precise structural architecture resulting in improved mechanical properties compared to conventional foams [1–3]. Inspiration for these attempts comes from natural materials, such as bone, antlers, carapaces, beaks, and bamboo stem, which exhibit superior mechanical properties when compared to artificial foams. Solid and cellular components, e.g., prismatic (hexagonal) and polyhedral cells found in wood, cork or trabecular bone, are arranged in specific structures resulting in a unique combination of stiffness and strength [4,5]. The arrangement of building blocks is also affected by external stimuli (mechanical load exerted on structures) causing reinforcement of the natural structures where it is needed during the growth (adaptive growth) and lifetime (remodelling). While the adaptive growth just deposits the material in a specific manner (e. g. wood), the remodelling comprises both deposition and removal of the material (e. g. bone) and requires the presence of living cells [6]. Functional foams with porosity (or density) gradient found in the bamboo plant are an example of such structure, where the porosity gradient also results in a gradation of properties [7,8]. Notably, the cell walls are often formed by nanoparticle (NP) reinforced biopolymers, which local mechanics also depends on the structural arrangement at the nanoscale [9–11]. Recreation of such structures may benefit from the investigation of NP spatial arrangement strategies in polymer matrices [12–14]. Seemingly, the overall mechanical performance is governed by the overall cell size, shape, and spatial distribution rather than by the exact chemical composition of the cell wall [4,7,15].

Therefore, current efforts are also focused on the preparation of artificial woods, putting emphasis on the oriented channel formation and strong defect-free walls [16]. Although the method of freeze-casting demonstrated a feasible preparation process for oriented channels, it was shown difficult to prepare the walls with at least similar strength as natural woods [17]. The insufficient penetration of light inside the frozen material, which should initiate the photo-polymerization of the channels' supports, requires an additional thermal cross-linking, which violates the channel orientation. Nevertheless, the provided concept

* Corresponding author.
E-mail address: xcsvatik@vutbr.cz (J. Svatík).

https://doi.org/10.1016/j.polymertesting.2021.107405
Received 1 April 2021; Received in revised form 22 September 2021; Accepted 28 October 2021
Available online 1 November 2021

offers another inspiration for hierarchical nature-inspired structures [16]. An example of a very efficient bio-mimicking structure already implemented in current materials (in automotive or spacecraft industry) is a sandwich structure, which consists of two thin plates carrying the load and a thick light core linking these plates transferring shear stress. Such structure was found in human skull, and the core of sandwich, usually having a honeycomb structure, comes from the honeybee's comb [4,18]. The honeycomb structure showed to be very efficient in stress absorption and possesses low density, which led to its use in novel lightweight materials for stress dampening, e. g., for electric vehicle battery housing [19]. The research of honeycomb structural parameters regarding mechanical properties, such as corner radius, interface between arrays of hexagonal cells, or coping with varying thickness of cell walls, is still ongoing [20]. Another attempts to fabricate artificial functionally graded materials include syntactic foams (polymer matrix filled with hollow glass spheres) [21–23], controlled physical foaming [24,25] or graded porous materials prepared by a microfluidic technique [1,26,27].

Recently, many studies have focused on the emerging 3D printing technologies using various materials (polymers or polymer composites), which can be used for the fabrication of simple geometrical objects but also very complex architectures [28–32]. There are various 3D printing techniques widely available, e. g., stereolithography apparatus (SLA) for liquid resin printing [33–35], selective laser sintering (SLS) for powder printing [36] or fused deposition modelling (FDM), which deposits thermoplastic polymer filament [37,38]. The advantages of the last technique are its versatility, simplicity, availability of commercial filaments and printers, ability to print internally closed cells, and almost no need for post-processing unless a very fine structure is desired [39]. The spatial resolution of the technology is given by the nozzle diameter and visco-elastic properties of the polymer material printed.

To improve mechanical properties of printed objects, there is an ongoing effort to modify the internal structure of printed bodies, widely referred to as *infill*, so that the mechanical properties are maximally enhanced at the given material composition. Bates et al. [29,40] manufactured honeycomb structures for energy absorbing applications from thermoplastic polyurethanes (TPUs) using FDM and tailored the specimen density, resulting in an anisotropic density gradient. They reported different onsets of stress plateau regions for four different density gradient honeycomb structures in compressive tests. Furthermore, they concluded that the continuous density gradient denoted the least well-defined plateau region due to the overlapping strain regions of two consecutive density layers, i.e., that the higher density layer started to deform while the lower density layer was not yet fully compressed. This phenomenon was confirmed in a study by Dawei et al. [41] who investigated sheet-based and strut-based gyroid cellular structures with two different density gradients. Uniform density gyroids showed global collapse deformation, whereas density gradient gyroids deformed in a layer-by-layer manner. Furthermore, energy absorption diagrams and impact energy tests both confirmed that the graded structures absorbed low and high impact energies better and intermediate impact energy less well than uniform density structures. Anisotropic character of the structure was found to play an important role, as the isotropic sheet-based gyroid structure showed higher absorption energy than anisotropic strut-based gyroid structure. Examination of damping properties showed that the loading direction also had a significant effect on the absorbed energy and the structures damped more energy when compressed in the transverse direction than in the ribbon direction. Kucewicz et al. [42,43] investigated two different printing orientations of dumbbells and showed lower yield stress under uniaxial stress for vertically printed samples in comparison with horizontally printed ones. Apparently, this was caused by discontinuities between the inner layers and boundary layers leading to small and large gaps in the horizontally and vertically printed samples, respectively. Investigations by Wang et al. [44] focused on the impact of raster orientation and the width of a single printing line on the mechanical properties of 3D printed parts. Specimens with raster orientations of 0° and 45° (with respect to the *x*-axis) created less micropores between adjacent lines than 90° and 0°/90° orientations, thus, reaching higher values of Young's modulus and strength in tension. Furthermore, a higher number of narrower printing lines is required compared to wider printing lines to cover the same area, which led to more micropores and worsened mechanical properties.

Polylactic acid (PLA) is a biodegradable polymer, produced from renewable resources and widely used for 3D printing due to its good processability and properties [45,46]. However, PLA is very susceptible to physical ageing [47–50] because its T_g (62 °C) is close to room temperature. All polymers undergo physical ageing [51]. Fast polymer processing with a relatively rapid melt cooling compared to the rather long chain relaxation times leads to a non-equilibrium state of the glassy phase below the glass transition temperature (T_g). Although the polymer coil reorganization is then arrested, segmental scale motions are still possible. Considering the potential energy landscape paradigm [52,53], energy maxima can be imagined as mountains and energy minima as valleys. Their organization immediately after processing depends on the processing protocol and change during ageing in dependence on the relative position of ageing temperature to the T_g. During ageing, energy minima are deepened, which can cause a significant change in macroscopic properties [54,55].

Fatal embrittlement of PLA accompanied by increase of Young's modulus and yield stress were observed after only a few hours of ageing at room temperature as elongation decreased from several hundreds to approximately 5% and catastrophic failure replaced ductile yielding in uniaxial tension [48–50,56]. It was proven that the observed behaviour was not connected to crystallization or chemical degradation [48,49]. Instead, the PLA ageing phenomenon was correlated with the enthalpy relaxation caused by physical ageing. Such deterioration of properties limits its suitability for advanced applications. To overcome this drawback, PLA has been toughened by blending with another polymer, plasticization, or copolymerization [50,56,57]. However, this can further increase the price of PLA, reduce biodegradability, or worsen its 3D printing processability together with some other properties.

Therefore, the nature-inspired design mimicking the bamboo stem structure was combined with the known 3D printing processing-macrostructure function to investigate the structural toughening of PLA without modifying its chemical composition. Three types of bio-inspired gradient porosity structures were compared with bodies with rectilinear infill pattern and infill density ranging from 20 to 100%. 3D printed specimens were subjected to a three-point bending mechanical tests and the results were compared with samples with isotropically organized pores. The design induced a transition from brittle failure to a quasi-ductile stress-strain response with suppressed catastrophic breakup and improved mechanical performance. The introduction of the bioinspired toughening mechanism by the 3D printed porosity gradient was observed for the first time. Moreover, the results did not correlate with the predictions of the Ashby and Gibson model for porous materials which suggests a need for novel theoretical concepts to be sought for these innovative 3D structures.

2. Materials and methods

2.1. Specimens preparation

Non-porous, uniform porosity, and gradient porosity specimens were 3D printed by a FDM printer (Rebel II, Czech Republic) using a commercial polylactic acid (PLA) filament 'PLA natural' (Gembird, Netherlands) with a glass transition temperature of 62 °C and melting temperature of 170 °C (measured by DSC Discovery, TA Instruments, USA). The nozzle and heatbed temperatures were 215 °C and 55 °C, respectively, while printing the first layer, and 200 °C and 50 °C, respectively, for the rest of the print. A 0.4 mm diameter nozzle was used. Specimen dimensions were (8 × 8 × 160) mm^3. Solid specimens

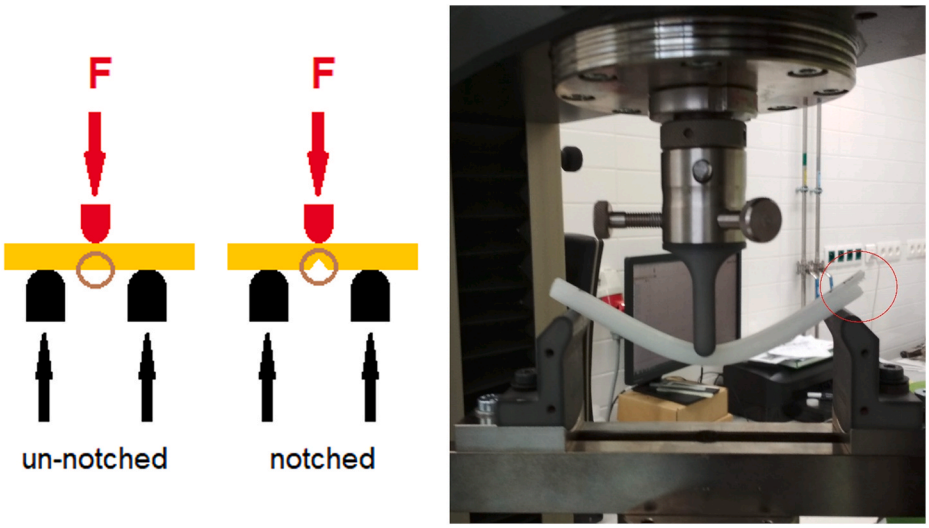

Fig. 1. A scheme of experimental testing (left) and an image of real-time three-point bending test of un-notched 3D printed specimen (right) – a delamination can be seen in the red circle. (For interpretation of the references to colour in this figure legend, the reader is referred to the Web version of this article.)

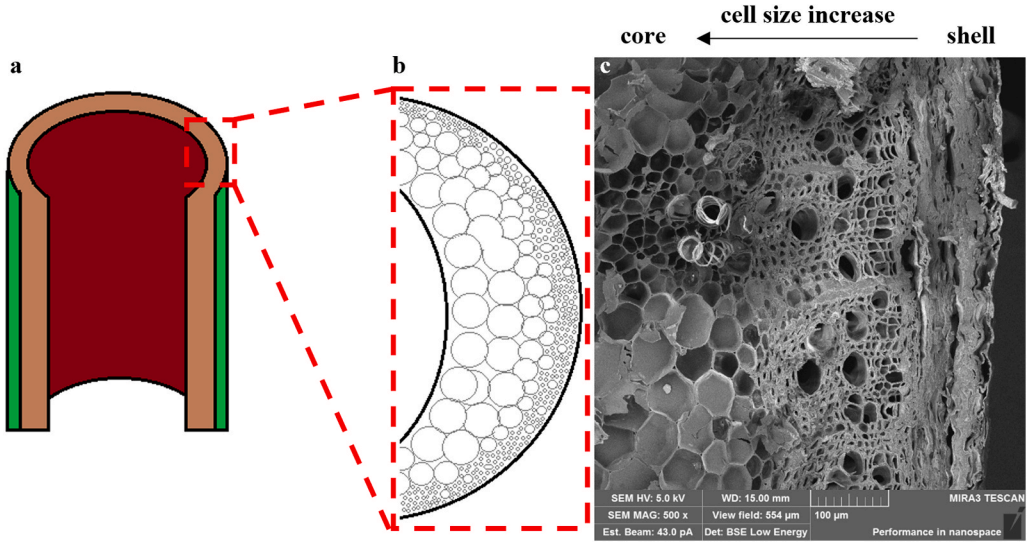

Fig. 2. a. Scheme of bamboo stem with a detail (b.) of the porosity gradient; c. SEM image of bamboo-grass stem with the porosity gradient (scale bar – 100 µm).

(100% infill) are denoted as 'non-porous', uniform porosity specimens with isotropically organized pores as 80% full, 60% full, 40% full and 20% full, and porosity gradient specimens as gradient I, II and III.

It is noted that the indicated percentage of the uniform porosity specimens reflects the infill setting in the Slic3r software, not the actual porosity (see Table 1). Uniform porosity specimens were printed using the pre-programmed setting in the Slic3r software with a rectangular shape of cells. The porosity gradient specimens were designed in Fusion 360 (Autodesk, USA) and the design is discussed further on. The samples were aged at room temperature for a month before testing.

2.2. Analysis

A confocal laser scanning microscope (CLSM) Olympus LEXT OLS4100 (Olympus, Japan) with long working distance lenses and 20× magnification, and scanning electron microscope Mira3 XMU (Tescan, CZ) in the low vacuum UniVac mode were used to visualize the 3D printed structure. Mechanical testing in a 3-point bending setup (Fig. 1) at ambient conditions (23 °C, 0.1 MPa) was performed on a Zwick Z010 (Zwick-Roell, Germany) with 10 kN force sensor and support separation of 128 mm (80% of total length) at a deformation rate of 1 mm/min. Notched specimens were prepared (Driven Notchvis, CEAST, Germany) with a depth of 45% of the specimen's width (3.6 mm). Density (ρ) was measured as the ratio of the specimen mass (m_s) to the specimen volume (V_s) obtained from the outer dimensions of the specimens (w – width, h – height, l – length):

$$\rho = \frac{m_s}{V_s} = \frac{m_s}{w \cdot h \cdot l} \quad (1)$$

Values normalized to the density of a non-porous specimen were used as a measure of porosity.

3. Results and discussion

The bamboo-grass stem structure (Fig. 2) was used as a bio-inspiration for the design of three porosity gradients (Fig. 3c) [58]. Mechanical robustness of the fast-growing bamboo is attributed to its graded internal porous structure where the cell dimension rises from the shell to the core. This type of gradation was adapted into our specimens where the porosity rose almost linearly from the edge to the centre but

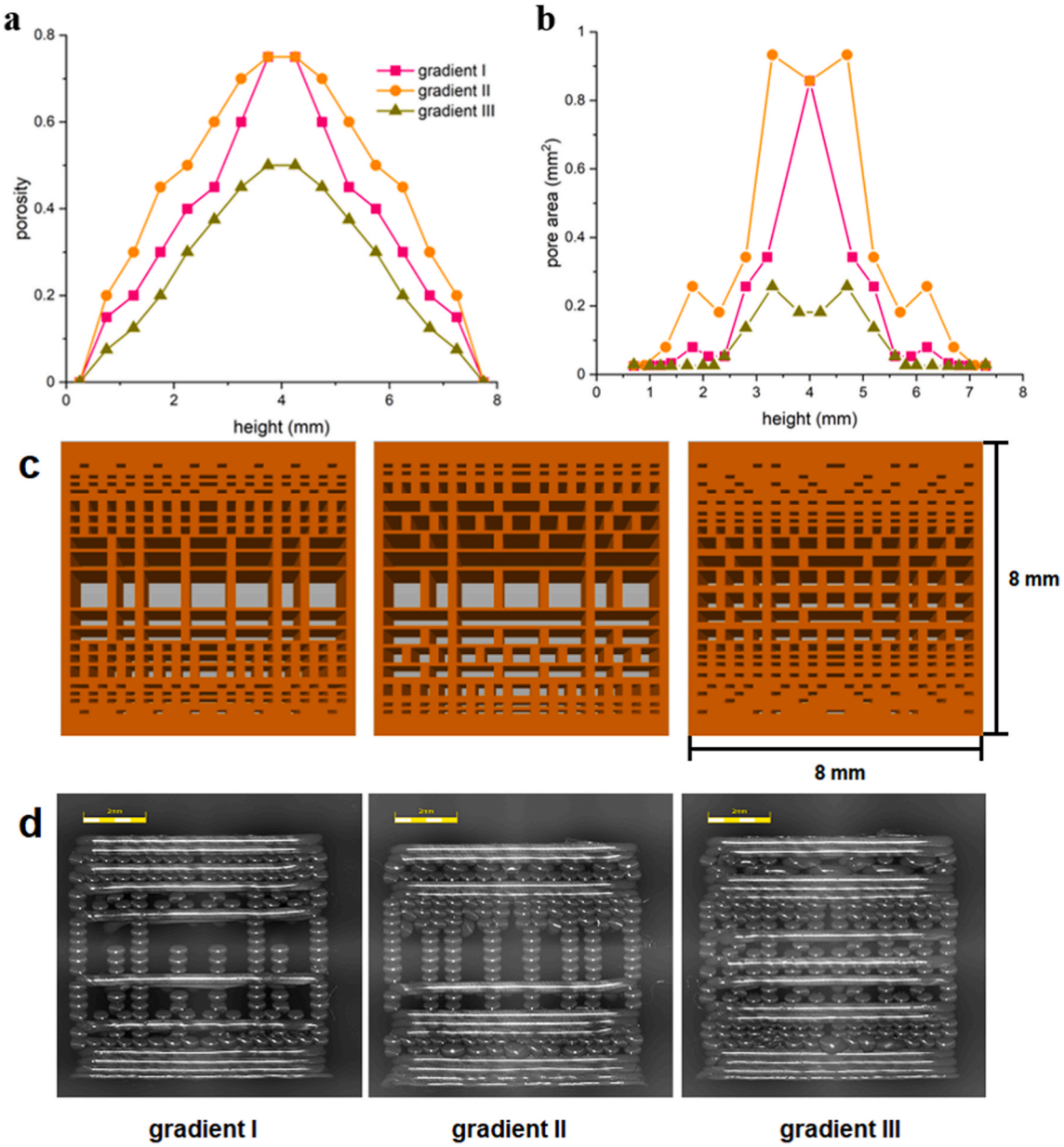

Fig. 3. Porosity trend (a.) and average area of a single pore (b.) in gradient specimens with respect to their placement across the specimen height (the lines are just guides for the eye); c. Design detail of the gradient specimens investigated in the *x*-*z* plane; d. CLSM images of gradient 3D printed samples (scale bar is 2 mm).

reached different values for various gradients (Fig. 3a). However, the specific cell distribution as well as sizes varied in each gradient (Fig. 3c) to observe any differences in mechanical response related to the cell arrangement while the porosity values were kept rather similar. A basic building block (cell) of the 3D printed porosity gradient designs had been defined as a rectangular shaped block with (0.25 × 0.1) mm^2 (*x* vs *z*) dimensions which was assembled into bigger blocks creating larger pores (Fig. 4). The cells were empty in the direction of specimens' length (*y* axis) and no porosity gradient or additional cellular structure was designed in this direction.

Cellular structure and porosity gradient were present in the *x* and *z* directions, only, and the pore area distribution is depicted in Fig. 3b.

Some dissimilarity between the models and actual structures (Fig. 3c and d) was caused by the limited spatial resolution of the printer equipped with a 0.4 mm nozzle. However, the bioinspired gradient structure was kept in all three cases. Moreover, the mechanical response clearly demonstrated that this approach successfully altered the material performance even for somewhat imperfect structures (Figs. 5 and 3d, respectively). As was mentioned before [44], the gaps between adjacent printing lines and layers affect the mechanical properties of the printed structure and their distribution can be controlled by raster orientation. However, the printing pattern in this case was very specific and macropores intentionally created within the structure had a more significant impact on mechanical properties than gaps. Thus, a 45°/–45° raster orientation was chosen for the solid layers (100% filled) in non-porous specimens and uniform porosity specimens, and the top and bottom layers in porosity gradient specimens, to avoid inconsistencies between adjacent printing lines. In the case of porosity gradient specimens, a raster orientation of 0° was used due to their specific cell distribution to avoid additional gaps. The sample indication, density, and mechanical properties are listed in Table 1.

Mechanical properties of graded structures reported in the literature [29,40–42] focused solely on compressive loading where the specimens did not break but underwent densification. In contrast, the load in a three-point bending test is divided into three parts – compressive at the top, shear in the middle, and tensile at the bottom. Three-point bending

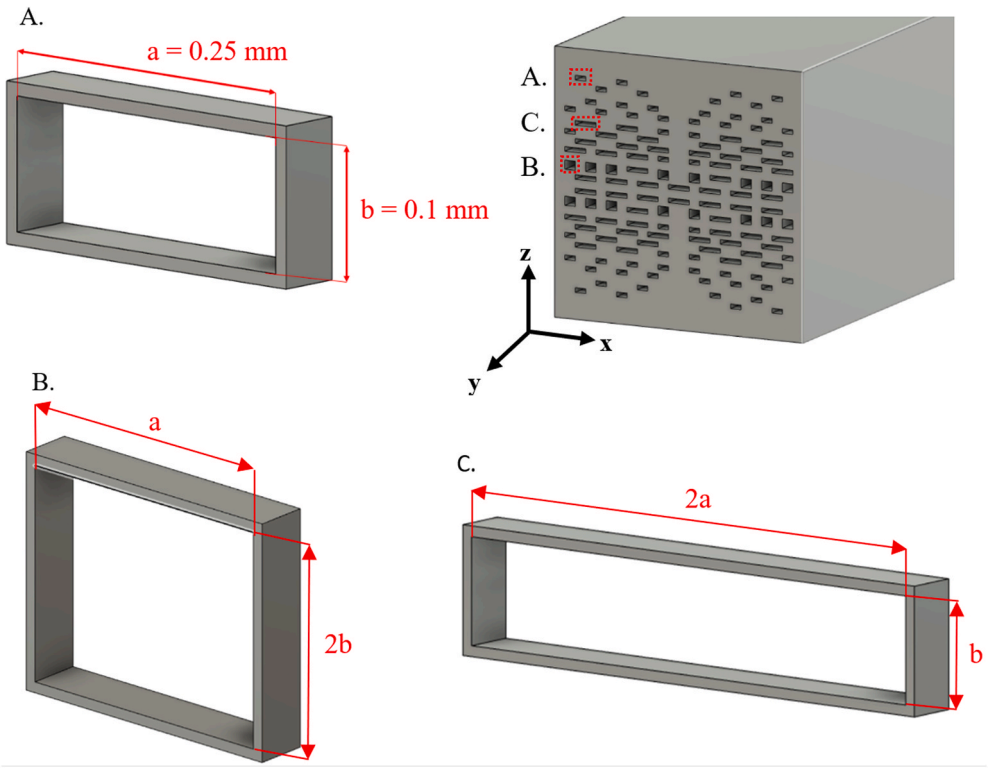

Fig. 4. A scheme of the basic unit cell (A.) with dimensions and indicated placement within the design; two further examples (B. and C.) of cells showing how they were derived from the basic unit cell with indicated dimensions; the *x, y*, and *z* axes depict the orientation of cells within the porosity design with respect to the printing area where *x-y* plane represents the heatbed area, and *z*-axis is the height of specimen.

is more relevant to many structural applications and allows investigation of the failure mode. The gradient structures were compared with non-porous and uniform porosity systems. A principal difference was observed in the mechanical stress-strain response (Fig. 5). The composition, processing parameters, and ageing time were the same for all samples. Moreover, analysis of the moment of inertia showed that it was negligibly affected by the internal porosity. Therefore, the changes were caused only by the structural design.

The solid specimen and the uniform porosity specimens showed brittle behaviour ending in a catastrophic breakup, whereas the gradient porosity specimens exhibited a quasi-ductile character (SI1) with no catastrophic breakup and significantly higher strain at break (Fig. 5). Several jumps were observed for graded specimens' mechanical response, where each jump represented a gradual stress growth in a layer with the subsequent layer collapse accompanied by local failure [29,41]. The central part of the gradient porosity structures was weakened because of the large pores and thin walls. Therefore, the highest stress was concentrated in the thinnest walls in the middle of the sample, which collapsed first. The stress transferred from the collapsed wall to the stronger neighbouring layer, which was able to support the stress for longer. The introduction of these sacrificial layers, which prevented catastrophic failure, can be taken as a macroscopic analogy of sacrificial bonds in biological systems [58,59]. However, no analogy of the hidden length was present in the prepared structures. Therefore, a significant decrease of the yield stress was observed.

The failure mechanism of porous AM structures was also investigated in Ref. [60], where a collapse of a porous structure was recorded with the deformation of every single layer characterized by an independent stress-strain diagram. Similar phenomenon was observed where each leap of the stress-strain curve was attributed to the collapse of a single layer, which prolonged the deformation curve resulting in quasi-ductile failure mechanism. Here, the apparent yield stress and strain at break were fully dependent on the design and distribution of cells. Hence, after reaching the apparent yield stress, a further increase in stress was observed, which could be attributed to the deformation of smaller pores with thicker walls. The gradient III structure collapsed with brittle fracture after progressive deformation, whereas the gradient I and II samples exhibited a continuous decrease of stress without macroscopic breakup until the end of the test was reached at 80% drop of the maximum force (Fig. 5).

The uniform porosity samples showed a gradual decrease of yield stress without any increase of maximum strain, as expected. Over two and a half times higher maximum strain was reached for the gradient I and II specimens than for non-porous specimens. However, the increase for the gradient III was smaller (about 1.5%). This difference could possibly be attributed to a lower number of smaller pores and the overall denser structure of gradient III compared to gradients I and II. The collapse of small central pores could not delocalize the stress as effectively as in the case of larger pores, thus, the structure behaved more like non-porous and uniform porosity specimens leading to a brittle catastrophic failure at lower strain values than in the gradient I and II specimens. The pores were directly responsible for the energy dissipation through the weak sacrificial bonds represented by the thin walls separating the pores, which caused the inter-layer delamination and prevented the crack to propagate through the whole thickness of the specimen. Hence, despite the local brittle failure, the overall mechanical response of the macroscopic bodies resembled the behaviour of ductile materials with the maximum elongation shifted to much higher strains without the catastrophic failure taking place. Gradients I and II diverted the crack growth most effectively, while the structure of gradient III was less effective but reached higher strength, all due to the pore distribution and pore sizes. However, the precise mechanism behind the porosity gradients' (pore distribution, pore sizes) mechanical response is not entirely clear and will be subjected to further investigations. Other porosity designs were prepared with different printing nozzle diameter and porosity trend to tune the mechanical response and also to confirm

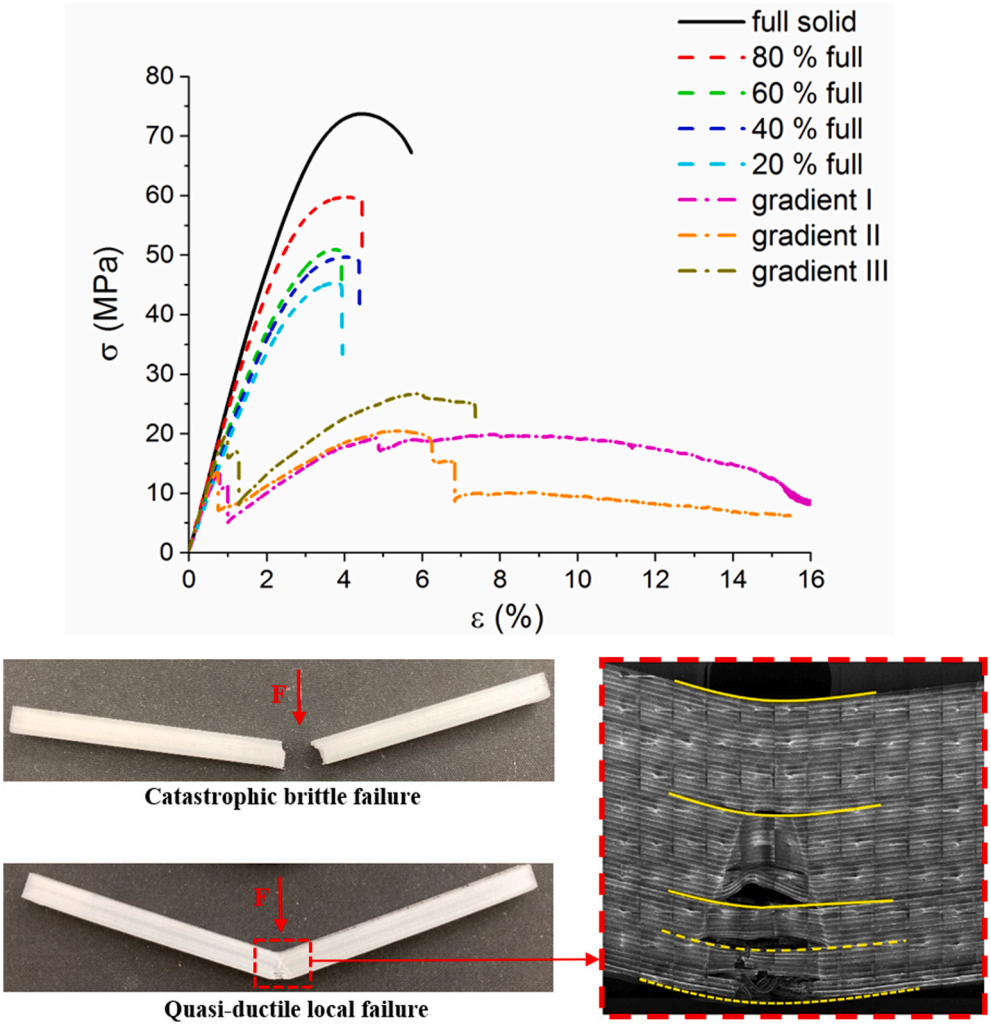

Fig. 5. Stress-strain curves of PLA samples with various porosity and 3D printed design deformed in three-point bending (top). Comparison of failure modes of specimens after 3-point bending test with an SEM image detail of quasi-ductile local failure (bottom) – red arrows indicate the direction of the acting force (F), full yellow lines indicate intact layers, dashed lines indicate gradually failing layers. (For interpretation of the references to colour in this figure legend, the reader is referred to the Web version of this article.)

Table 1
Sample indication, density, and selected mechanical properties.

	indication	density [g•cm^{-3}]	relative density [g•cm^{-3}]	yield strength [MPa]	Young's modulus [MPa]	maximum strain [%]
solid	non-porous	1.111	1	74.0	2433	5.7
uniform	80% full	1.023	0.92	60.0	2339	4.5
	60% full	0.916	0.82	50.5	2030	3.5
	40% full	0.842	0.76	49.7	1940	4.4
	20% full	0.722	0.65	44.4	1889	3.1
gradient	gradient I	0.887	0.80	21.0	2128	13.7
	gradient II	0.773	0.70	12.5	2098	15.5
	gradient III	0.875	0.79	21.1	2320	7.4

the importance of structural design. After the three-point bending test, even higher yield strength for the new porosity trends was recorded compared to the solid specimen (SI2). The investigated structural designs could also inspire an improvement of mechanical robustness of scaffolds prepared by 3D bioprinting.

The relative Young's modulus and relative bending strength of the uniform porosity specimens exhibited a linear increase from the lowest to the highest relative density due to the increasing volume of material as expected (Fig. 6). A theoretical prediction from the Ashby and Gibson models [4] was compared with the experimental results of 3D printed uniform and gradient porosity structures. These models were designed for cubic-shaped cells repeating in the whole specimen and creating a regular network of cells, which is quite similar to the uniform porosity structures in the present work, where rectangular cells are repeated with different size to control the level of infill. Gradient porosity structures also contained rectangular cells but with size varying over the *z*-direction. Specific mechanical properties were calculated according to equations (2) and (3), creating theoretical model data based on the relative density of the porous structures relative to non-porous bodies (Fig. 6).

The relative Young's modulus was calculated as:

$$\frac{E^*}{E_s} = C_1 \cdot (\frac{\rho^*}{\rho_s})^2 \quad (2)$$

where E^* and E_S are the Young's moduli of the porous and solid structure, respectively, C_1 is a geometric constant, and ρ^* and ρ_s are the densities of the porous and solid material, respectively. Relative bending strength was calculated as:

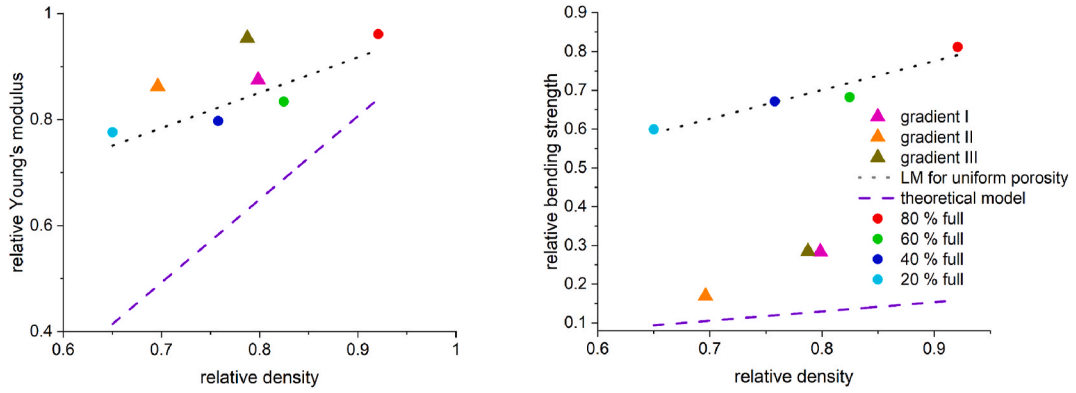

Fig. 6. Relative Young's modulus (left) and relative bending strength (right) with respect to the relative density of the foams; LM stands for linear model; error bars are included in dimensions of the marks in the diagrams.

Table 2
Experimental geometric constants related to the cell geometry calculated values and values suggested (SV) in the literature (Ashby, Gibson [4]).

	uniform porosity				gradient porosity			SV
	80% full	60% full	40% full	20% full	type I	type II	type III	
C_1	1.134	1.227	1.388	1.837	1.374	1.781	1.538	1
C_2	0.919	0.911	1.018	1.144	0.398	0.291	0.407	0.18

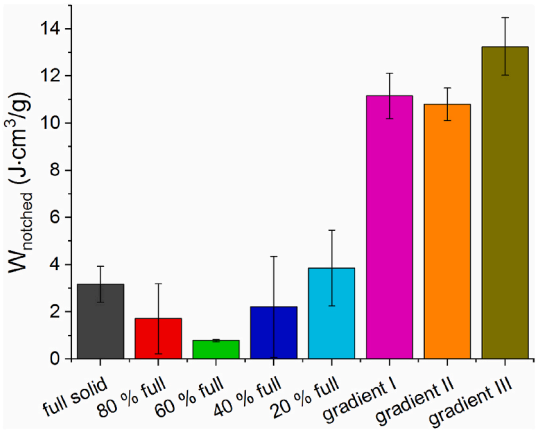

Fig. 7. Work to failure in three-point bending of notched 3D printed specimens with various porosity designs.

$$\frac{\sigma_f}{\sigma_s} = C_2 \cdot \left(\frac{\rho^*}{\rho_s}\right)^{3/2} \quad (3)$$

where σ_f and σ_s are bending strengths of the porous and solid structure, respectively, and C_2 is a geometric constant. The geometric constants ($C_{1\text{-}2}$) are essential parameters for the prediction of mechanical properties and the experimental data for the 3D printed systems investigated are shown in Table 2. These results could be compared to the data suggested in the literature [4]; nevertheless, the standard model yields much lower $C_{1\text{-}2}$ values than the experimentally fitted ones (Table 2 and Fig. 6). Apparently, the specific 3D printing design does not conform well to the Ashby and Gibson models for cellular materials. A significant difference between the mechanical performance of uniform and gradient porosity structures was obvious.

The values of relative Young's modulus of gradient II and III specimens exceeded even the linear trend of uniform porosity specimens. On the contrary, the relative bending strength of porosity gradient specimens fell behind the uniform porosity samples due to the weak central part consisting of thin cell walls and large cells. Nevertheless, these values still exceeded the predictions of the standard Ashby and Gibson models. The comparison of the experimental data with the theoretical model suggested that it could be beneficial to modify the model parameters for 3D printed cellular structures. The essential discrepancy could lie in the inherent outer solid shell with no macroscopic porosity of the 3D printed design, which could significantly alter the stress distribution during deformation. Notched samples were tested (SI3) to overcome this issue by disrupting the outer shell and assessing the performance of the inner design. The work to failure of notched specimens was evaluated from the three-point bending tests (Fig. 7). The mechanical energy needed for the failure of the uniform porosity and solid samples lay within the experimental error. However, more than 4 times greater values were determined for all types of gradient porosity design. This proved that the specific bioinspired 3D printed design can toughen brittle polymers such as aged PLA.

4. Conclusion

The toughening of PLA achieved via structurally bioinspired 3D printed design without altering the chemical composition was reported for the first time. Preparation of porous structures using 3D printing proved to be a suitable way for the production of precisely distributed cells for controlled mechanical performance. Three types of gradient porosity structures were designed inspired by structure of bamboo stem. The design of cell size and wall thickness appeared to be the key variables when considering the bending strength, work to break, strain at break, failure mode, and Young's modulus of the structures. The bending strength was reduced due to large cells and thin cell walls in the central layers. However, the gradient porosity structures reached far higher values of maximum strain than both solid and uniform porosity structures and showed a shift from brittle failure to a quasi-ductile behaviour with no catastrophic breakup in both cases. Comparison of the experimental data with the theoretical models from Ashby and Gibson showed significant discrepancies, not only for the gradient porosity structures, but also for the uniform porosity structures. It was suggested that the outer solid shell inherent in 3D design essentially changed the stress distribution during the deformation of the cellular structures. Therefore, notched samples were tested to investigate the influence of the inner 3D printed design. The work at break of the notched gradient specimens significantly exceeded that of the solid and uniform porosity samples due to the altered stress distribution and crack propagation. The local failure and gradual collapse of individual cell layers, followed by stress transfer into the neighbouring layer, were assumed to be analogous to the sacrificial bond toughening mechanism. The utilization of the toughening mechanisms found in biostructures via specific organization of 3D printed structures opens new possibilities for toughening of materials without chemical modification.

Author statement

Juraj Svatík: conceptualization, formal analysis, investigation, visualization, writing – original draft; Petr Lepcio: conceptualization, formal analysis, investigation, supervision, visualization, writing – review & editing; František Ondreáš: conceptualization, funding acquisition, supervision, writing – review & editing; Klára Zárybnická: investigation; Marek Zbončák: investigation, writing – review & editing; Přemysl Menčík: methodology; and Josef Jančář conceptualization.

Data availability

The raw/processed data required to reproduce these findings cannot be shared at this time due to time limitations and ongoing research study.

Declaration of competing interest

The authors declare that they have no known competing financial interests or personal relationships that could have appeared to influence the work reported in this paper.

Acknowledgments

We greatly acknowledge the financial support from LTAUSA19059 Inter-Excellence Grant from MEYS CR. We also acknowledge CzechNanoLab Research Infrastructure supported by MEYS CR (LM2018110).

References

[1] M. Costantini, J. Jaroszewicz, Ł. Kozoń, K. Szlązak, W. Święszkowski, P. Garstecki, C. Stubenrauch, A. Barbetta, J. Guzowski, 3D-Printing of functionally graded porous materials using on-demand reconfigurable microfluidics, Angew. Chem. Int. Ed. 58 (2019) 7620–7625, https://doi.org/10.1002/anie.201900530.
[2] N. Kanu, U. Vates, G. Singh, S. Chavan, Fracture problems, vibration, buckling, and bending analyses of functionally graded materials: a state-of-the-art review including smart FGMS, Part. Sci. Technol. 37 (2019) 583–608, https://doi.org/10.1080/02726351.2017.1410265.
[3] C. Cramer, T. Aguirre, T. Holland, K. Ma, Prediction of continuous porosity gradients in ceramics using ZnO as a model material, J. Am. Ceram. Soc. 102 (2018) 587–594, https://doi.org/10.1111/jace.15872.
[4] L. Gibson, M. Ashby, B. Harley, Cellular Materials in Nature and Medicine, First, Cambridge University Press, New York, 2010.
[5] L. Gibson, Biomechanics of cellular solids, J. Biomech. 38 (2005) 377–399, https://doi.org/10.1016/j.jbiomech.2004.09.027.
[6] R. Weinkamer, P. Fratzl, Mechanical adaptation of biological materials — the examples of bone and wood, Mater. Sci. Eng. C 31 (2011) 1164–1173, https://doi.org/10.1016/j.msec.2010.12.002.
[7] D. Wu, F. Xu, B. Sun, R. Fu, H. He, K. Matyjaszewski, Design and preparation of porous polymers, Chem. Rev. 112 (2012) 3959–4015, https://doi.org/10.1021/cr200440z.
[8] M. Esmailzadeh, H. Danesh Manesh, S. Zebarjad, Fabrication and characterization of functional graded polyurethane foam (FGPUF), Polym. Adv. Technol. 29 (2018) 182–189, https://doi.org/10.1002/pat.4100.
[9] M. Zboncak, F. Ondreas, V. Uhlir, P. Lepcio, J. Michalicka, J. Jancar, Translation of segment scale stiffening into macroscale reinforcement in polymer nanocomposites, Polym. Eng. Sci. 60 (2019) 587–596, https://doi.org/10.1002/pen.25317.
[10] J. Jancar, F. Ondreas, P. Lepcio, M. Zboncak, K. Zarybnicka, Mechanical properties of glassy polymers with controlled NP spatial organization, Polym. Test. 90 (2020), https://doi.org/10.1016/j.polymertesting.2020.106640.
[11] F. Ondreas, P. Lepcio, M. Zboncak, K. Zarybnicka, L. Govaert, J. Jancar, Effect of nanoparticle organization on molecular mobility and mechanical properties of polymer nanocomposites, Macromolecules 52 (2019) 6250–6259, https://doi.org/10.1021/acs.macromol.9b01197.
[12] P. Lepcio, F. Ondreáš, K. Zárybnická, M. Zbončák, J. Svatík, J. Jančář, Phase diagram of bare particles in polymer nanocomposites: uniting solution and melt blending, Polymer 230 (2021), https://doi.org/10.1016/j.polymer.2021.124033.
[13] K. Zarybnicka, F. Ondreas, P. Lepcio, M. Kalina, M. Zboncak, J. Jancar, Thermodynamic parameters controlling nanoparticle spatial packing in polymer solutions, Macromolecules 53 (2020) 8704–8713, https://doi.org/10.1021/acs.macromol.0c00698.
[14] P. Lepcio, F. Ondreas, K. Zarybnicka, M. Zboncak, O. Caha, J. Jancar, Bulk polymer nanocomposites with preparation protocol governed nanostructure: the origin and properties of aggregates and polymer bound clusters, Soft Matter 14 (2018) 2094–2103, https://doi.org/10.1039/C8SM00150B.
[15] B. Koohbor, A. Kidane, Design optimization of continuously and discretely graded foam materials for efficient energy absorption, Science (Wash. D C) 102 (2016) 151–161, https://doi.org/10.1016/j.matdes.2016.04.031.
[16] Z. Yu, B. Qin, Z. Ma, Y. Gao, Q. Guan, H. Yang, S. Yu, Emerging bioinspired artificial woods, Adv. Mater. 33 (2021), https://doi.org/10.1002/adma.202001086.
[17] S. Deville, Freezing Colloids: Observations, Principles, Control, and Use: Applications in Materials Science, Life Science, Earth Science, Food Science, and Engineering, 1 ed., Springer International Publishing, Cham, 2017.
[18] T. Khan, V. Acar, M. Aydin, B. Hülagü, H. Akbulut, M. Seydibeyoğlu, A review on recent advances in sandwich structures based on polyurethane foam cores, Polym. Compos. 41 (2020) 2355–2400, https://doi.org/10.1002/pc.25543.
[19] M. Mudassir, F. Tarlochan, M. Mansour, Nature-inspired cellular structure design for electric vehicle battery compartment: application to crashworthiness, Appl. Sci. 10 (2020), https://doi.org/10.3390/app10134532.
[20] D. Goss, Y. Mistry, S. Niverty, C. Noe, B. Santhanam, C. Ozturk, C. Penick, C. Lee, N. Chawla, A. Grishin, V. Shyam, D. Bhate, Bioinspired honeycomb core design: an experimental study of the role of corner radius, coping and interface, Biomimetics 5 (2020), https://doi.org/10.3390/biomimetics5040059.
[21] N. Gupta, A functionally graded syntactic foam material for high energy absorption under compression, Mater. Lett. 61 (2007) 979–982, https://doi.org/10.1016/j.matlet.2006.06.033.
[22] N. Gupta, S. Zeltmann, V. Shunmugasamy, D. Pinisetty, Applications of polymer matrix syntactic foams, JOM 66 (2014) 245–254, https://doi.org/10.1007/s11837-013-0796-8.
[23] A. Singh, B. Saltonstall, B. Patil, N. Hoffmann, M. Doddamani, N. Gupta, Additive manufacturing of syntactic foams: Part 2: specimen printing and mechanical property characterization: Part 2, JOM 70 (2018) 310–314, https://doi.org/10.1007/s11837-017-2731-x.
[24] Q. Zhang, H. Lu, N. Kawazoe, G. Chen, Preparation of collagen porous scaffolds with a gradient pore size structure using ice particulates, Mater. Lett. 107 (2013) 280–283, https://doi.org/10.1016/j.matlet.2013.05.070.
[25] J. Yu, L. Song, F. Chen, P. Fan, L. Sun, M. Zhong, J. Yang, Preparation of polymer foams with a gradient of cell size: further exploring the nucleation effect of porous inorganic materials in polymer foaming, Mater. Today Commun. 9 (2016) 1–6, https://doi.org/10.1016/j.mtcomm.2016.08.006.
[26] S. Andrieux, W. Drenckhan, C. Stubenrauch, Generation of solid foams with controlled polydispersity using microfluidics, Langmuir 34 (2018) 1581–1590, https://doi.org/10.1021/acs.langmuir.7b03602.
[27] J. Elsing, A. Quell, C. Stubenrauch, Toward functionally graded polymer foams using microfluidics, Adv. Eng. Mater. 19 (2017), https://doi.org/10.1002/adem.201700195.
[28] S. Shi, Y. Chen, J. Jing, L. Yang, Preparation and 3D-printing of highly conductive polylactic acid/carbon nanotube nanocomposites via local enrichment strategy, RSC Adv. 9 (2019) 29980–29986, https://doi.org/10.1039/C9RA05684J.
[29] S. Bates, I. Farrow, R. Trask, 3D printed polyurethane honeycombs for repeated tailored energy absorption, Mater. Des. 112 (2016) 172–183, https://doi.org/10.1016/j.matdes.2016.08.062.
[30] D. Rigotti, A. Dorigato, A. Pegoretti, 3D printable thermoplastic polyurethane blends with thermal energy storage/release capabilities, Mater. Today Commun. 15 (2018) 228–235, https://doi.org/10.1016/j.mtcomm.2018.03.009.
[31] N. Gama, A. Ferreira, A. Barros-Timmons, 3D printed cork/polyurethane composite foams, Mater. Des. 179 (2019), https://doi.org/10.1016/j.matdes.2019.107905.
[32] M. Lei, W. Hong, Z. Zhao, C. Hamel, M. Chen, H. Lu, H. Qi, 3D printing of auxetic metamaterials with digitally reprogrammable shape, ACS Appl. Mater. Interfaces 11 (2019) 22768–22776, https://doi.org/10.1021/acsami.9b06081.
[33] H. Eng, S. Maleksaeedi, S. Yu, Y. Choong, F. Wiria, C. Tan, P. Su, J. Wei, 3D stereolithography of polymer composites reinforced with orientated nanoclay, Procedia Eng. 216 (2017) 1–7, https://doi.org/10.1016/j.proeng.2018.02.080.
[34] Z. Weng, Y. Zhou, W. Lin, T. Senthil, L. Wu, Structure-property relationship of nano enhanced stereolithography resin for desktop SLA 3D printer, Compos. Appl. Sci. Manuf. 88 (2016) 234–242, https://doi.org/10.1016/j.compositesa.2016.05.035.
[35] R. Farahani, M. Dubé, D. Therriault, Three-dimensional printing of multifunctional nanocomposites: manufacturing techniques and applications, Adv. Mater. 28 (2016) 5794–5821, https://doi.org/10.1002/adma.201506215.
[36] Selective Laser Sintering (SLS) - Parts on Demand, Stratasys., 2020. https://www.stratasysdirect.com/technologies/selective-laser-sintering. accessed 2020-02-29.
[37] V. Mazzanti, L. Malagutti, F. Mollica, FDM 3D printing of polymers containing natural fillers: a review of their mechanical properties, Polymers 11 (2019), https://doi.org/10.3390/polym11071094.
[38] S. Tronvoll, T. Welo, C. Elverum, The effects of voids on structural properties of fused deposition modelled parts: a probabilistic approach, Int. J. Adv. Manuf. Technol. 97 (2018) 3607–3618, https://doi.org/10.1007/s00170-018-2148-x.
[39] J. Stansbury, M. Idacavage, 3D printing with polymers: challenges among expanding options and opportunities, Dent. Mater. 32 (2016) 54–64, https://doi.org/10.1016/j.dental.2015.09.018.
[40] S. Bates, I. Farrow, R. Trask, Compressive behaviour of 3D printed thermoplastic polyurethane honeycombs with graded densities, Mater. Des. 162 (2019) 130–142, https://doi.org/10.1016/j.matdes.2018.11.019.
[41] D. Li, W. Liao, N. Dai, Y. Xie, Comparison of mechanical properties and energy absorption of sheet-based and strut-based gyroid cellular structures with graded densities, Materials 12 (2019), https://doi.org/10.3390/ma12132183.
[42] M. Kucewicz, P. Baranowski, J. Małachowski, A. Popławski, P. Płatek, Modelling, and characterization of 3D printed cellular structures, Mater. Des. 142 (2018) 177–189, https://doi.org/10.1016/j.matdes.2018.01.028.

[43] M. Kucewicz, P. Baranowski, J. Małachowski, A method of failure modeling for 3D printed cellular structures, Mater. Des. 174 (2019), https://doi.org/10.1016/j.matdes.2019.107802.
[44] Wang Zhao, Fuh Lee, Effect of porosity on mechanical properties of 3D printed polymers: experiments and micromechanical modeling based on X-ray computed tomography analysis, Polymers 11 (2019), https://doi.org/10.3390/polym11071154.
[45] M. Vert, J. Mauduit, S. Li, Biodegradation of PLA/GA polymers: increasing complexity, Biomaterials 15 (1994) 1209–1213, https://doi.org/10.1016/0142-9612(94)90271-2.
[46] W. Liu, J. Zhou, Y. Ma, J. Wang, J. Xu, Fabrication of PLA filaments and its printable performance, IOP Conf. Ser. Mater. Sci. Eng. 275 (2017), https://doi.org/10.1088/1757-899X/275/1/012033.
[47] H. Cai, V. Dave, R. Gross, S. McCarthy, Effects of physical aging, crystallinity, and orientation on the enzymatic degradation of poly(lactic acid), J. Polym. Sci. B Polym. Phys. 34 (1996) 2701–2708, https://doi.org/10.1002/(SICI)1099-0488(19961130)34:16<2701::AID-POLB2>3.0.CO;2-S.
[48] L. Cui, B. Imre, D. Tátraaljai, B. Pukánszky, Physical ageing of Poly(Lactic acid): factors and consequences for practice, Polymer 186 (2020), https://doi.org/10.1016/j.polymer.2019.122014.
[49] P. Pan, B. Zhu, Y. Inoue, Enthalpy relaxation and embrittlement of poly(l -lactide) during physical aging, Macromolecules 40 (2007) 9664–9671, https://doi.org/10.1021/ma071737c.
[50] I. Haugan, B. Lee, M. Maher, A. Zografos, H. Schibur, S. Jones, M. Hillmyer, F. Bates, Physical aging of polylactide-based graft block polymers, Macromolecules 52 (2019) 8878–8894, https://doi.org/10.1021/acs.macromol.9b01434.
[51] G. McKenna, Physical Aging in Glasses and Composites, Long-Term Durability of Polymeric Matrix Composites, 2012, pp. 237–309, https://doi.org/10.1007/978-1-4419-9308-3_7.
[52] S. Sastry, P. Debenedetti, F. Stillinger, Signatures of distinct dynamical regimes in the energy landscape of a glass-forming liquid, Nature 393 (1998) 554–557, https://doi.org/10.1038/31189.
[53] P. Debenedetti, F. Stillinger, Supercooled liquids and the glass transition, Nature 410 (2001) 259–267, https://doi.org/10.1038/35065704.
[54] H. Meijer, L. Govaert, Mechanical performance of polymer systems: the relation between structure and properties, Prog. Polym. Sci. 30 (2005) 915–938, https://doi.org/10.1016/j.progpolymsci.2005.06.009.
[55] F. Ondreas, J. Jancar, Temperature, frequency, and small static stress dependence of the molecular mobility in deformed amorphous polymers near their glass transition, Macromolecules 48 (2015) 4702–4716, https://doi.org/10.1021/acs.macromol.5b00550.
[56] G. Zhao, F. Gomes, H. Marway, M. Thompson, Z. Zhu, Physical aging as the driving force for brittle–ductile transition of polylactic acid, Macromol. Chem. Phys. 221 (2019), https://doi.org/10.1002/macp.201900475.
[57] K. Anderson, K. Schreck, M. Hillmyer, Toughening polylactide, Polym. Rev. 48 (2008) 85–108, https://doi.org/10.1080/15583720701834216.
[58] W. Huang, D. Restrepo, J. Jung, F. Su, Z. Liu, R. Ritchie, J. McKittrick, P. Zavattieri, D. Kisailus, Multiscale toughening mechanisms in biological materials and bioinspired designs, Adv. Mater. 31 (2019), https://doi.org/10.1002/adma.201901561.
[59] G. Fantner, E. Oroudjev, G. Schitter, L. Golde, P. Thurner, M. Finch, P. Turner, T. Gutsmann, D. Morse, H. Hansma, P. Hansma, Sacrificial bonds and hidden length: unraveling molecular mesostructures in tough materials, Biophys. J. 90 (2006) 1411–1418, https://doi.org/10.1529/biophysj.105.069344.
[60] J. Kadkhodapour, H. Montazerian, A. Darabi, A. Anaraki, S. Ahmadi, A. Zadpoor, S. Schmauder, Failure mechanisms of additively manufactured porous biomaterials: effects of porosity and type of unit cell, J. Mech. Behav. Biomed. Mater. 50 (2015) 180–191, https://doi.org/10.1016/j.jmbbm.2015.06.012.